ACS OMEGA

http://pubs.acs.org/journal/acsodf

Article

Research on the Pollutant Migration Law Based on Large-Scale Three-Dimensional Similar Simulation Experiments of Underground Coal Gasification

Lin Xin,* Kaixuan Li, Mingze Feng, Weimin Cheng, Zhigang Wang, Jiaze Li, and Jing Wu

Cite This: *ACS Omega* 2022, 7, 15982−15995

Read Online

ACCESS | Metrics & More | Article Recommendations

ABSTRACT: The potential pollution risk of underground coal gasification (UCG) has become a key factor restricting the development of UCG industrialization. Therefore, studying the migration and diffusion behavior of harmful pollutants is of great significance for preventing UCG pollution. In this paper, a large-scale three-dimensional similar simulation experimental device for UCG is used to simulate the gasification of Tianjin fat coal under actual working conditions. The rock layer around the simulated coal seam was sampled after the gasification was completed, the contaminants in the samples were examined by XRD, and the changes in the relative content of the contaminants at different sampling points were studied by FTIR. The results showed that benzene, phenols, aldehydes, aromatic hydrocarbons, and aromatic heterocyclic compounds remained after the gasification of No. 7 sampling point in Qianjiang, Tianjin, and that the main pollutants were aromatic hydrocarbons. The migration and enrichment of phenol and aldehyde pollutants were about the same on the east and west sides of the gasification center, while benzene pollutants were more easily migrated and enriched than aromatic heterocyclic compounds. The migration distance of phenolic pollutants on the south side of the gasification area is smaller than that of other pollutants and their maximum vertical distance from the gasification reaction area to the south is about 0.7 m. The results can provide a scientific basis for pollutant risk identification and prevention and control in the later UCG field test.

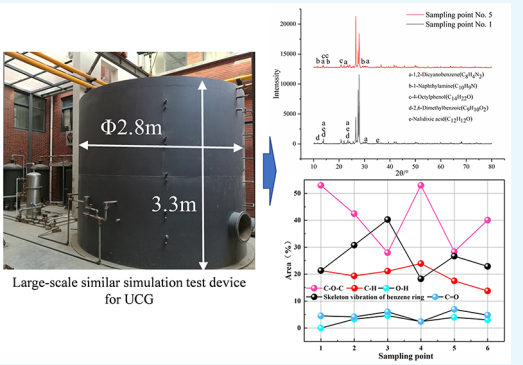

Large-scale similar simulation test device for UCG

1. INTRODUCTION

According to BP's "2016 World Energy Statistics Report", from the perspective of global fossil energy reserves, there are abundant coal, oil, and natural gas reserves.[1,2] Especially for coal resources, the current reserve-production ratio has reached 114 years.[3] In particular, in China, the characteristics of its resource occurrence can be summarized as "rich coal, lack of oil, and less gas" in general, which determines that China's energy structure will be dominated by coal for a long period of time.[4] Therefore, using coal resources safely, cleanly, and efficiently has become an urgent problem to be solved. Underground coal gasification (UCG), as a coal in situ utilization technology, can not only recover and utilize low-rank coal seams that cannot be economically mined or are difficult to mine by traditional coal mining technology[5−7] but can also be an effective method for mining coal seams with high sulfur, high ash, high gas, residual coal, and deep coal seam.[8] As a result, it has received more and more attention from countries.[9−11]

However, an important issue that cannot be ignored is the pollution caused by UCG (Figure 1). In the process of UCG, the temperature of the oxidation zone can reach above 1100 °C and the surrounding rocks around the coal seam will produce pores and cracks under the action of high temperature and high pressure.[12] The coal gas produced by gasification (in addition to H_2, CO, CH_4, and other combustible components, it contains benzene, naphthalene, phenol, polycyclic aromatic hydrocarbons, and other organic pollutants) may enter the aquifer through these pores and fissures to pollute groundwater. In addition, when the gasification is finished, a large amount of cooling water should be introduced into the combustion space area until the combustion space area is filled with water. At this time, the alkaline oxide in the residual coal ash after gasification is leached under groundwater immersion, increasing the pH value of water and the concentration of inorganic components (mainly harmful trace elements).[13] However, there is still a lack of identification and evaluation of underground environmental pollutants, which has become a key factor restricting the industrialization of UCG.

Received: February 25, 2022
Accepted: April 8, 2022
Published: April 26, 2022

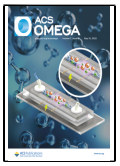

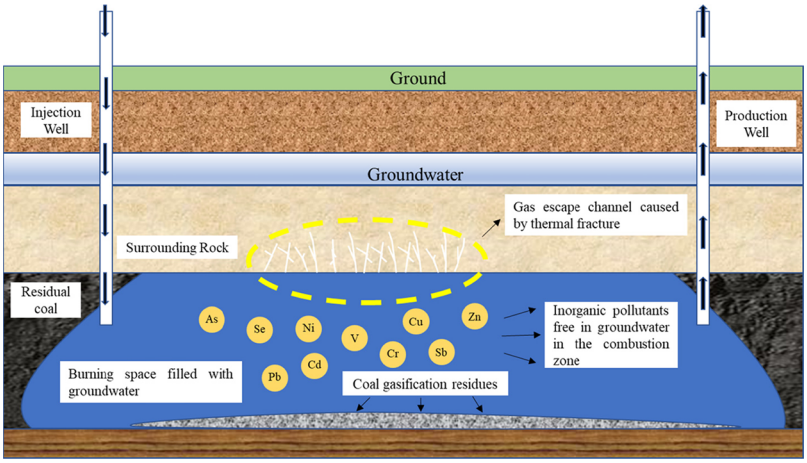

Figure 1. Schematic diagram of pollutants after UCG.

In this regard, many scholars have conducted a large number of theoretical and experimental studies on the pollution problems caused by the UCG technology. Li et al. took lignite as the research object and established the functional relationship between pyrolysis temperatures and pollutants by simulating the precipitation process of pollutants from UCG.[14] Krzysztof Kapusta and others conducted a two-week onsite UCG experiment at the "Barbara" mine in Poland.[15] They conducted extensive research on the formation, release, and migration of pollutants. Ütnü et al. analyzed Malkara lignite (Turkey) and the ash generated from underground gasification and studied the composition of polycyclic aromatic hydrocarbons and their derivatives and the distribution of organic matter in the samples.[16] Ma et al. prepared the continuous conversion product of UCG through a pyrolysis device and combined chemical analysis and thermodynamic calculation to study the chemical forms of the harmful elements in the UCG product.[17] In addition, a risk assessment code (RAC) is introduced to evaluate the risk level of harmful trace elements in the underground environment. Liu et al. used a direct drilling method to detect the combustion space of an underground borehole gasifier, studied the migration range and characteristics of the pollutants, and explored the migration path of the pollutants.[18] Ye et al. conducted gasification experiments on Hebi bituminous coal using a two-stage method and discussed the effects of gasification products and residues on groundwater.[19] Many scholars simulated the process of UCG through self-made experimental equipment for simulating UCG.[20,21] They conducted leaching research on the residual ash and coke from gasification. Study the migration and enrichment of harmful trace elements (Hg, As, Se, Cd, Pb, Ni, Zn, etc.) leached. Sadashivam et al. conducted laboratory underground gasification simulation experiments on coal in South Wales, studied the influence of gasification pollutants under different gasification process conditions, and used some measured parameters for theoretical calculations to predict the concentration of the main balance substances in the groundwater polluted by pollutants in the UCG process.[22] In addition, some scholars separated and extracted strains with high degradation activity toward phenol compounds from coking wastewater and domestic sewage and used the extracted strains to perform degradation experiments on gas washing water produced in the UCG model experiment to achieve the effect of pollutant degradation.[23]

In this paper, relying on the large-scale three-dimensional similar UCG simulation device in the resource underground gasification mining laboratory, the gasification simulation experiment of Qianjiaying Coal No. 7 coal was carried out and the gasification furnace body was dissected after the furnace was closed. The samples were analyzed by sampling the simulated rock layer around the coal seam (Figure 6a) using an X-ray diffractometer and Fourier infrared spectrometer. The types of pollutants produced during the UCG of Qianjiaying No. 7 coal and their migration and enrichment in the simulated rock strata are studied to provide a scientific basis for pollutant risk identification and prevention and control in the later UCG field test.

2. MATERIALS AND METHODS

2.1. Experimental Coal Sample. The coal selected for this gasification simulation experiment is fat coal taken from the No. 7 coal of the Qianjiaying Coal Mine (Figure 2). The calorific value of raw coal (unit MJ/kg) is between 21.25 and 27.99 and the average value of medium-heat coal is 25.16 (Table 1).

Figure 2. Qianjiaying Coal Mine No. 7 coal.

2.2. Simulating Device for UCG. The simulation device for UCG (Figure 3) consists of five parts: an experimental furnace body, an air supply and exhaust system, a gas acquisition and analysis system, an automatic temperature measurement system,

Table 1. Industrial Analysis of Coal (in percentage)[a]

A_d	V_{daf}	S_{td}	$Q_{gr.ad}$
27.91	20.83	0.41	25.16

[a] A_d = dry base ash, V_{daf} = dry without ash base volatiles, S_{td} = dry based total sulfur, $Q_{gr.ad}$ = high calorific value of coal.

https://doi.org/10.1021/acsomega.2c01135
ACS Omega 2022, 7, 15982−15995

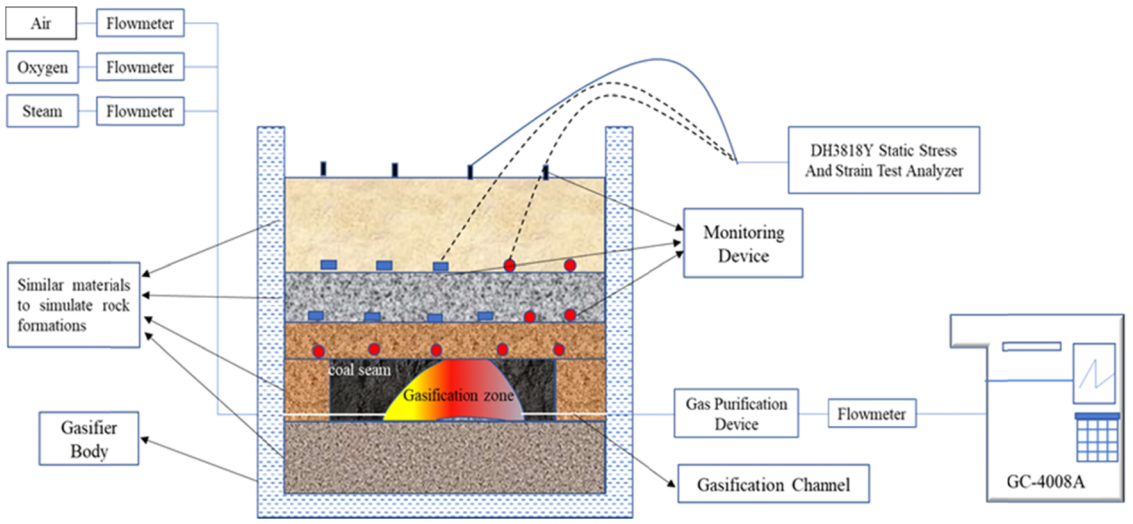

Figure 3. Schematic diagram of a gasification furnace for a UCG simulation experiment.

and a monitoring system. Among them, the principal part is the experimental furnace body, which is a cylindrical structure with an external diameter of 3.73 m and a height of 3.54 m and is provided with a certain thickness of refractory and thermal insulation materials inside. According to the similarity theory, the experiments were conducted by laying similar materials in layers inside the furnace to simulate the rock layer around the coal seam, and monitoring devices such as thermocouples, pressure boxes, and displacement gauges were preset inside the simulated rock layer. The process gas components are detected by an online chromatograph GC-4008A dedicated to coal mines—the preset monitoring device records in real-time through a DH3818Y static stress and strain test and analysis system. DH3818Y is a static strain tester with an LCD screen, which includes three different configuration options of 8, 16, or 24 measuring channels.[24] Each measuring channel can measure force, displacement, or strain. During measurement, functions such as sampling control and data analysis are realized through LCD screens or computer software.

2.3. Coal Seam Simulation. The simulated structure of the coal seam is shown in Figure 4a, and a 35-cm-thick similar material is laid on the bottom of the gasification furnace body to serve as the coal seam floor. A simulated coal seam with a length of 1.2 m from north to south, a width of 0.6 m from east to west, and a thickness of 0.3 m is laid with lump coal on the upper part of the bottom plate and the gaps are filled with pulverized coal. At the same time, similar materials are laid around the coal seam, and gasification channels are preset with guard pipes at the bottom of the coal seam (Figure 4). After the coal seam and similar materials around the coal seam are laid, the simulated overburden of the coal seam shall be laid layer by layer according to different material ratios, and monitoring devices such as thermocouples, pressure box, and displacement meter shall be installed.

2.4. Experimental Method. The experiment simulated the horizontal single-channel underground gasification process. A gasification channel is arranged along the coal seam floor, and the gasification agent (air, oxygen, steam, and their mixture) is injected into the south side of the channel after the commissioning of all the devices is completed. At the same time, the switch is turned on and the heating plate embedded 0.3 m from the air inlet is ignited to ignite the coal seam. Whether

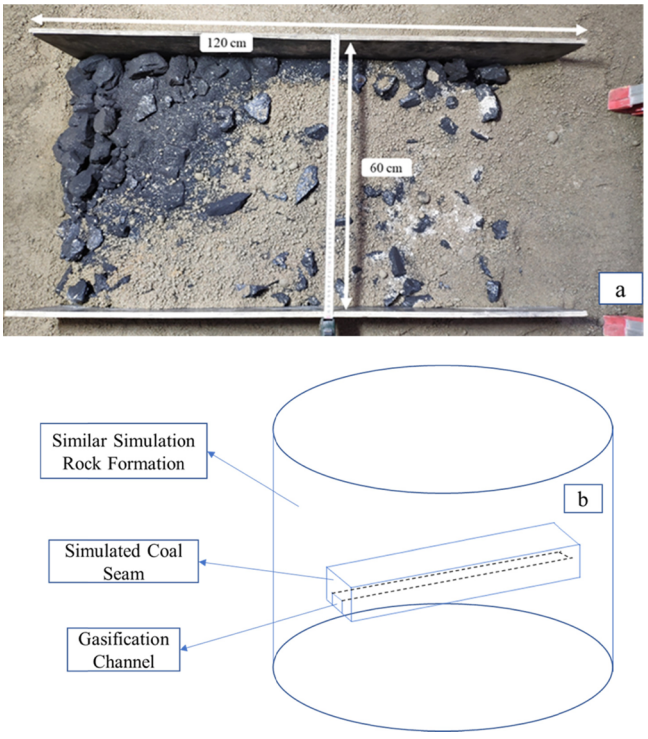

Figure 4. (a) Simulation of coal seam and (b) schematic diagram of the simulated coal seam in a gasifier.

the ignition is successful can be judged by monitoring the temperature and gas components. After successful ignition, gasification of the simulated coal seam is carried out to study its gas production by passing gasification agents of different concentrations (Table 2). During gasification, the furnace body is in a micropositive pressure state, and the pressure in the combustion space area is about 0.05 MPa. After the gasifier is cooled, the furnace body is dissected and sampled at different locations in the combustion goaf area and similar simulated rock strata (Figure 6). A Fourier infrared spectrometer was used to analyze the functional groups of the samples, and the contaminants in the samples were characterized by XRD (Figure 5).

https://doi.org/10.1021/acsomega.2c01135
ACS Omega 2022, 7, 15982−15995

Table 2. Partial Gasification Experiment Plan

air + steam continuous gasification experiment			
air flow (m^3/h)	steam flow (m^3/h)	steam oxygen ratio	running time (h)
10	3	1.43:1	2
10	6	2.86:1	2
10	10	4.76:1	2
10	15	7.14:1	2

2.5. Samples and Analysis. *2.5.1. Sampling Situation.* As shown in Figure 6a, after the simulation of the UCG experiment, samples of imitated surrounding rock around the coal seam were taken according to the interval (unit cm) and the position shown in the figure, and the samples were stored in sealed bags to prevent oxidation. Figure 6b shows the sampling situation in the gasifier after the UCG is simulated.

2.5.2. XRD Analysis. The sample was ground with an agate mortar, sieved to below 75 μm, and analyzed and tested with a high-performance, multifunctional powder crystal X-ray diffractometer (Ultima IV). Use Cu target, Kα radiation, a scan range of ~5°−80°, a scan speed of 6°/min, a voltage of 20 kV, a current of 20 mA, and a step distance of 0.1° to test the organic pollutants. Using Jade 6.0 (MDI, Livermore, CA, USA) combined with the substance standard powder diffraction data (PDF) provided by the Powder Diffraction Federation International Data Center (JCPDS-ICDD), the organic pollutants are qualitatively determined according to the standard analysis method and the samples are determined by their composition of organic pollutants.

2.5.3. FTIR Analysis. An FTIR spectrum analysis was carried out using a Fourier infrared spectrometer NICOLET380. The sample (Figure 6a) and potassium bromide (KBr) were mixed in a ratio of 1:150 and ground in an agate mortar. After the mixture was fully uniformly ground, it was placed in a mold and pressed into tablets at a pressure of about 10 MPa and pressurized for about 3 min. The sample is made into a thin sheet of thickness 0.1~1 mm and a diameter of 13 mm, placed on the sample holder, and placed in the sample chamber of the infrared spectrometer for testing. The scanning range of the instrument is 4000~400 cm^{-1}, the resolution is 4 cm^{-1}, and the number of scans is accumulated 32 times to obtain high-quality infrared spectra.

2.5.4. FTIR Data Processing. Considering that the sample's composition is relatively complex and contains a variety of functional groups, the contribution of the absorption bands of these functional groups to the infrared spectrum is relatively broad. Therefore, it is easy to generate superposition at a certain position to cause graph superposition. The amount of superposition is difficult to investigate in the absorption band of the infrared spectrum. For this reason, this paper uses the PeakFit software to determine the position and number of the initial unfolding fitting peaks according to the second derivative of the infrared spectrum.[25,26] The parameters of the absorption peak are adjusted and the residual sum of squares between the original spectrum and the fitted spectrum is used as the minimum objective function as the fitting standard for fitting. In this way, the peak unfolding graph and the absorption peak parameters of the sample were obtained. Then the type of functional group was determined, and the intensity of the absorption peak was calculated.

3. RESULTS AND DISCUSSION

3.1. XRD Analysis Results. Phase identifying is also called "phase qualitative analysis". Its basic principle is based on the following three principles: Any phase has its characteristic diffraction spectrum; the diffraction spectra of any two phases cannot be the same; and the diffraction peaks of multiphase samples are mechanical superpositions of each phase. Therefore, a "card library of known phases" is established through experimental measurement or theoretical calculation. All phases in the sample can be retrieved by comparing the spectrum of the measured sample with the "standard card" in the PDF card library.

A phase search of different sampling points found that silicon dioxide (SiO_2) and albite ($Na_2O{\cdot}Al_2O_3{\cdot}6SiO_2$) were the main phases and there was no significant change in other phases except the main phase (Figures 7 and 8). The contaminants contained in the simulated rock formations are much smaller than other substances in the simulated rock formations. Therefore, the main detection was of minor and minute phases in the phase search of organics (Figure 9). Benzene, polycyclic aromatic hydrocarbons, and some heterocyclic compounds (1,2-dicyanobenzene,2,6-dimethylbenzoic acid, 1-naphthylamine, naphthalidionic acid, etc.) were found in 12 sampling sites. Phenolic compounds (4-octyl phenol, etc.) were found in some

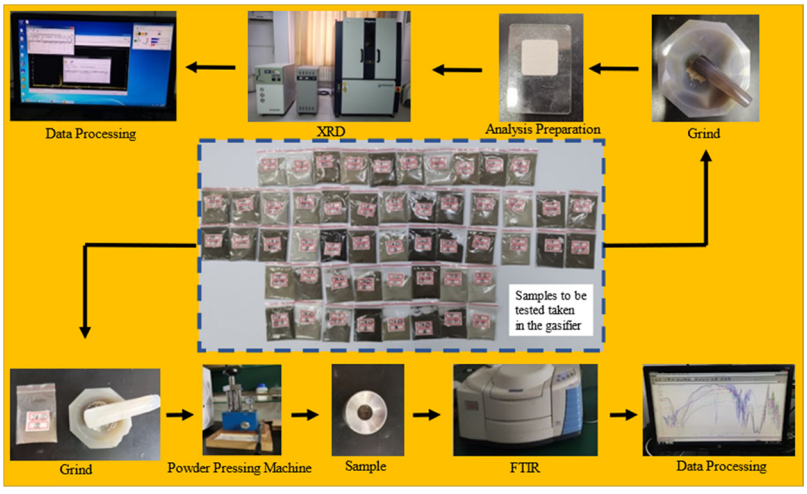

Figure 5. Sample test flow chart.

https://doi.org/10.1021/acsomega.2c01135
ACS Omega 2022, 7, 15982−15995

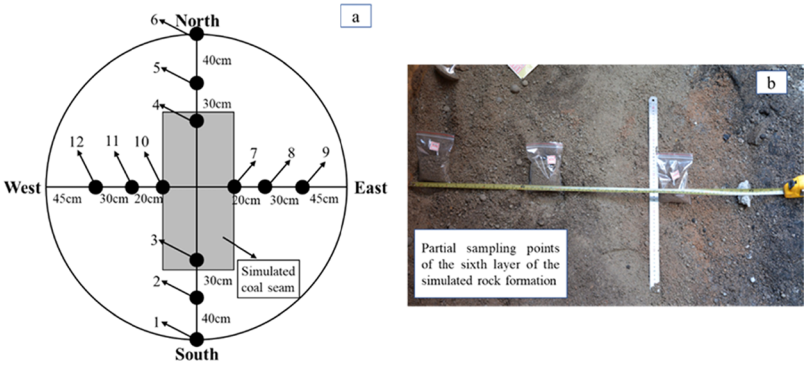

Figure 6. (a) Schematic diagram of the sampling of simulated rock formations around simulated coal seams and (b) simulated actual sampling of surrounding rock.

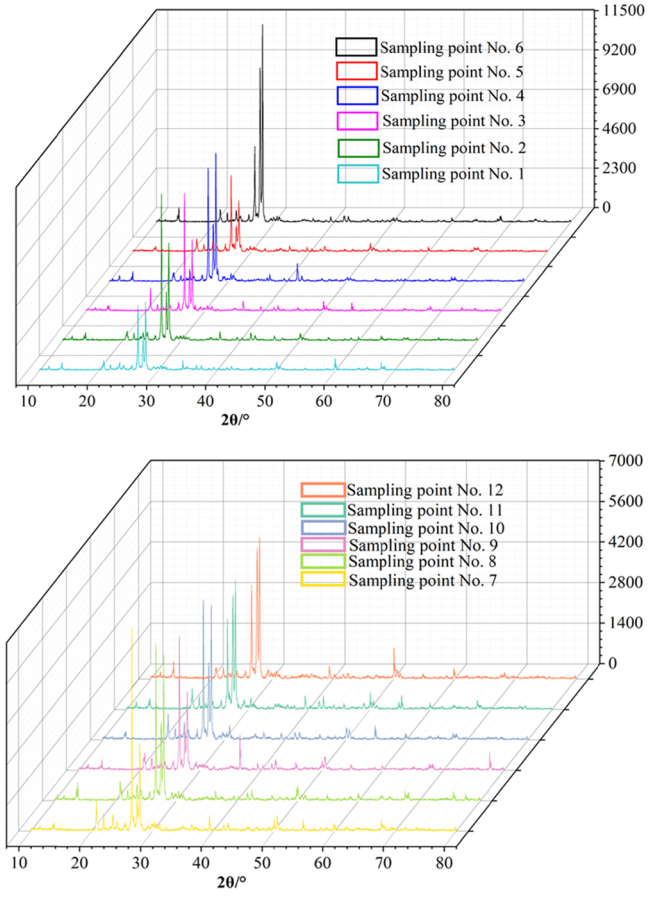

Figure 7. Smoothed XRD spectra of sampling points 1−12.

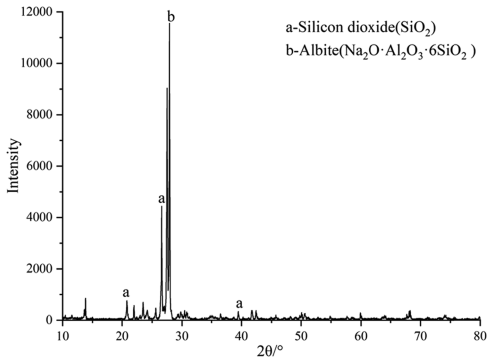

Figure 8. Sampling point No. 1.

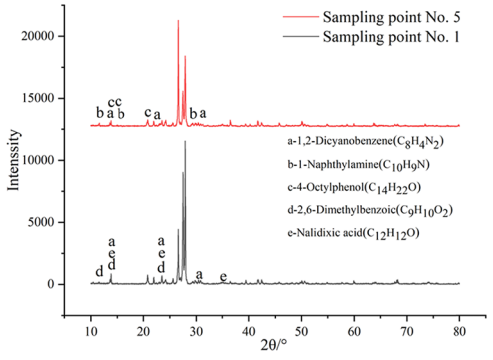

Figure 9. 1,5 pollutant situation at the sampling point.

sample sites. This indicates that the migration of phenolic pollutants is less than that of benzene and polycyclic aromatic hydrocarbons (PAHs).

3.2. FTIR Analysis Results. *3.2.1. Sampling and Analysis of Simulated Coal Seam Surrounding Rock.* Pollutants produced by UCG are similar to surface gasification beds. Inorganic pollutants mainly include hydrogen sulfide, ammonia, and harmful trace elements of heavy metals, while organic pollutants mainly include phenols, benzene, PAHs, heterocyclic compounds, etc.[27−29] In the experiment of simulating UCG, the simulated rock layer made of similar materials has a certain degree of adsorption. During gasification, the high-temperature coal gas will carry pollutants from the fissures into the surrounding rock layers and remain. For this reason, tools such as infrared spectroscopy can be used to study these pollutants at a microscopic level. Through FTIR detection of samples at sampling points, the type and relative content of the functional groups at each location can be determined to determine the contaminant migration and diffusion laws in the surrounding rock of coal seams.

Based on a large number of experiments and experiences, many scholars have summarized the types of absorption peaks in organic compounds and the assignment of their functional groups.[30−32] Due to the complex composition of the samples taken, the infrared spectrograms obtained are all superimposed by combining multiple functional groups. Therefore, to more clearly and accurately analyze the types of functional groups contained in the samples at the sampling points and their attributions, PeakFit and other software (the method described in Section 2.5.4) were used to perform fitting analysis on the obtained infrared spectra. By analyzing the changes of the

https://doi.org/10.1021/acsomega.2c01135
ACS Omega 2022, 7, 15982−15995

functional groups and their contents at each sampling point, the migration and diffusion of airborne pollutants in the surrounding rocks of the coal seam in the process of UCG are studied. Based on this, a 600−900 cm^{-1} aromatic hydrocarbon structure region and a 1000−1800 cm^{-1} oxygen-containing functional group region were selected to analyze and study the spectrogram (Figure 10).

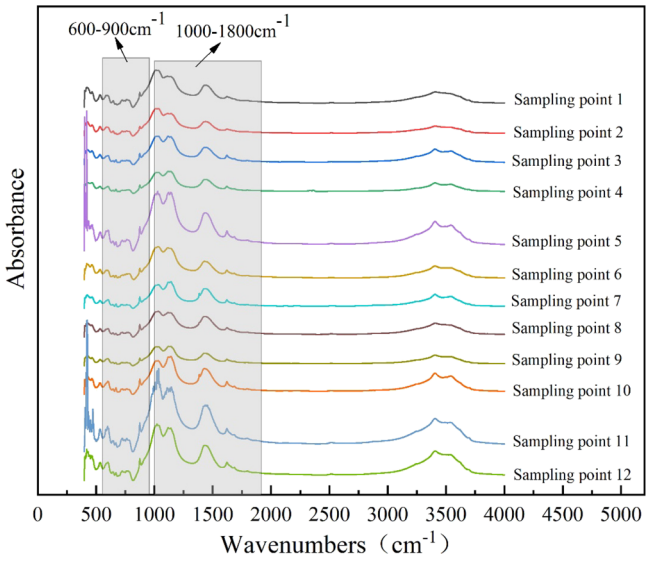

Figure 10. Infrared spectrum after processing.

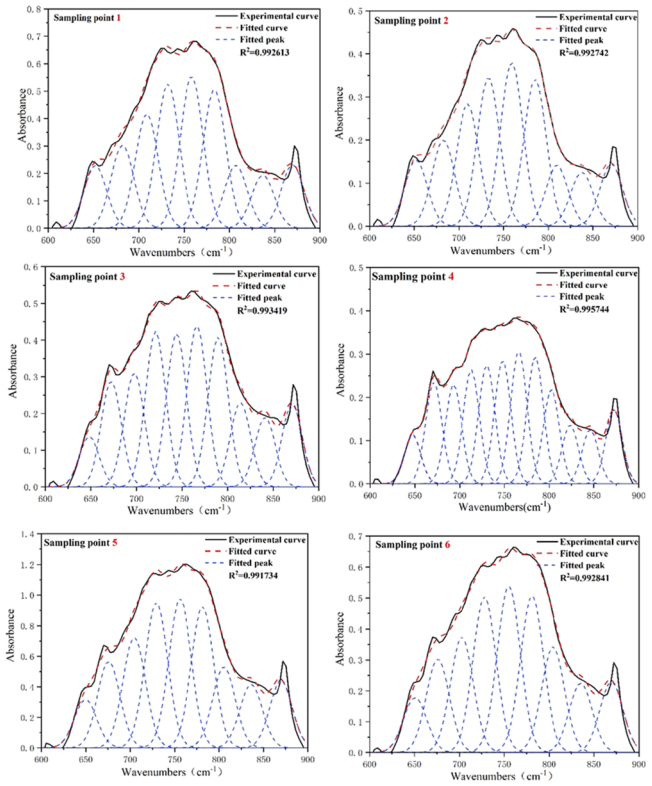

Figure 11. The fitting curve of 600−900 cm^{-1} sampling points 1−6.

3.2.2. Different Area Analysis. 3.2.2.1. Sampling Points 1−6, 600−900 cm^{-1} Sub-Peak. After the coal buried in the ground has undergone the process of underground gasification under different gasification agents, the harmful elements in the coal will

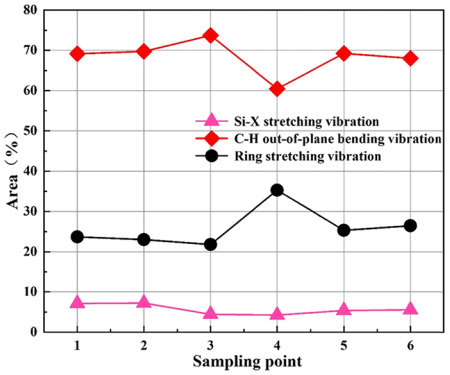

Figure 12. 600−900 cm^{-1} percentage of area.

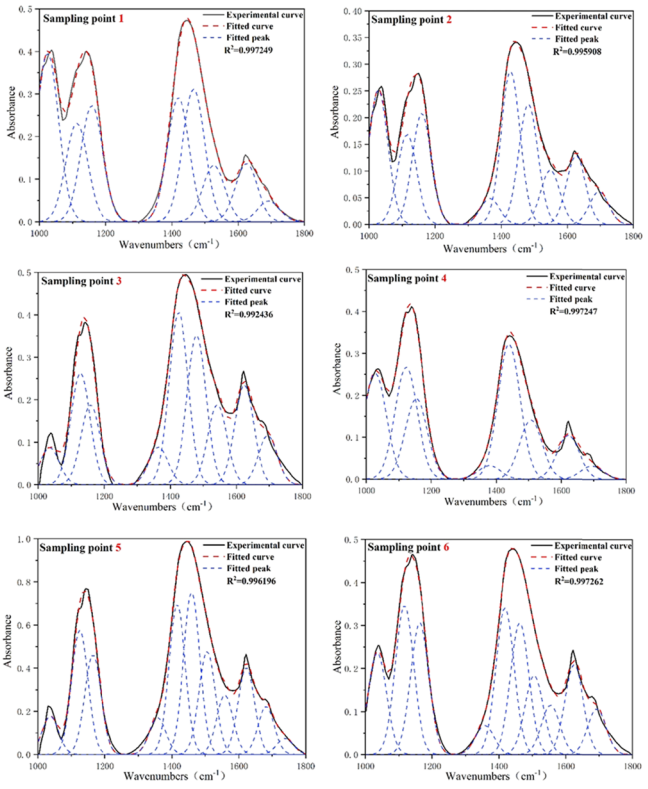

Figure 13. Fitting curve of 1000−1800 cm^{-1} sampling points 1−6.

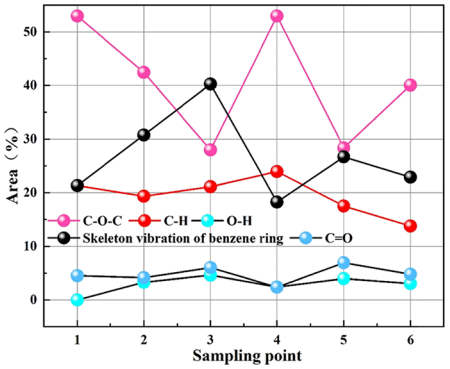

Figure 14. 1000−1800 cm^{-1} percentage of area.

be migrated and enriched to different degrees.[33,34] Some of the semivolatile elements, such as cadmium, copper, zinc, etc., have relatively small changes in element concentration before and

https://doi.org/10.1021/acsomega.2c01135
ACS Omega 2022, 7, 15982−15995

Table 3. Functional Group Attribution of 600−900 cm^{-1} at Sampling Points 1−6

sample point	center (cm^{-1})	area	area%	structure
sample point 1	652	7.173	7.16%	organic silicon compound Si−X stretching vibration
	682	9.510	9.49%	C−H bending vibration of m-disubstituted benzene
	709	13.116	13.08%	C−H bending vibration of monosubstituted benzene
	732	16.536	16.50%	aromatic heterocyclic ring stretching vibration
	758	17.439	17.40%	C−H bending vibration of monosubstituted benzene
	784	15.886	15.85%	C−H bending vibration of m-disubstituted benzene
	807	7.227	7.21%	aromatic heterocyclic ring stretching vibration
	837	6.089	6.07%	C−H bending vibration of p-disubstituted benzene
	870	7.267	7.25%	C−H bending vibration of pentasubstituted benzene
sample point 2	652	4.794	7.24%	organic silicon compound Si−X stretching vibration
	683	6.267	9.46%	C−H bending vibration of m-disubstituted benzene
	710	8.881	13.41%	C−H bending vibration of monosubstituted benzene
	733	10.806	16.32%	aromatic heterocyclic ring stretching vibration
	759	11.901	17.97%	C−H bending vibration of monosubstituted benzene
	785	10.684	16.13%	C−H bending vibration of m-disubstituted benzene
	810	4.426	6.68%	aromatic heterocyclic ring stretching vibration
	838	3.936	5.94%	C−H bending vibration of p-disubstituted benzene
	871	4.527	6.84%	C−H bending vibration of pentasubstituted benzene
sample point 3	648	3.780	4.46%	organic silicon compound Si−X stretching vibration
	672	7.953	9.38%	C−H bending vibration of benzene
	698	8.588	10.13%	C−H bending vibration of monosubstituted benzene
	721	11.656	13.75%	C−H bending vibration of m-disubstituted benzene
	744	11.545	13.61%	C−H bending vibration of monosubstituted benzene
	766	12.136	14.31%	aromatic heterocyclic ring stretching vibration
	790	11.265	13.28%	C−H bending vibration of m-disubstituted benzene
	814	6.362	7.50%	aromatic heterocyclic ring stretching vibration
	841	5.258	6.20%	C−H bending vibration of p-disubstituted benzene
	871	6.255	7.38%	C−H bending vibration of pentasubstituted benzene
sample point 4	647	2.568	4.25%	organic silicon compound Si−X stretching vibration
	671	5.347	8.84%	C−H bending vibration of benzene
	693	5.235	8.65%	C−H bending vibration of monosubstituted benzene
	713	5.998	9.92%	C−H bending vibration of m-disubstituted benzene
	730	6.263	10.35%	aromatic heterocyclic ring stretching vibration
	748	6.590	10.76%	C−H bending vibration of monosubstituted benzene
	766	6.990	11.56%	aromatic heterocyclic ring stretching vibration
	784	6.709	11.09%	C−H bending vibration of m-disubstituted benzene
	802	4.991	8.25%	aromatic heterocyclic ring stretching vibration
	824	3.105	5.13%	aromatic heterocyclic ring stretching vibration
	846	2.853	4.72%	C−H bending vibration of p-disubstituted benzene
	872	3.923	6.49%	C−H bending vibration of pentasubstituted benzene
sample point 5	650	10.072	5.42%	organic silicon compound Si−X stretching vibration
	676	18.003	9.69%	C−H bending vibration of benzene
	705	22.967	12.36%	C−H bending vibration of monosubstituted benzene
	729	30.204	16.26%	aromatic heterocyclic ring stretching vibration
	756	30.996	16.69%	C−H bending vibration of monosubstituted benzene
	781	29.330	15.79%	C−H bending vibration of m-disubstituted benzene
	806	16.854	9.07%	aromatic heterocyclic ring stretching vibration
	836	13.233	7.12%	C−H bending vibration of p-disubstituted benzene
	870	14.082	7.58%	C−H bending vibration of pentasubstituted benzene
sample point 6	651	5.745	5.58%	organic silicon compound Si−X stretching vibration
	676	9.753	9.47%	C−H bending vibration of benzene
	703	12.042	11.69%	C−H bending vibration of monosubstituted benzene
	728	16.178	15.71%	aromatic heterocyclic ring stretching vibration
	755	17.316	16.81%	C−H bending vibration of monosubstituted benzene
	781	16.301	15.83%	C−H bending vibration of m-disubstituted benzene
	804	11.045	10.72%	aromatic heterocyclic ring stretching vibration
	835	7.237	7.03%	C−H bending vibration of p-disubstituted benzene
	869	7.385	7.17%	C−H bending vibration of pentasubstituted benzene

https://doi.org/10.1021/acsomega.2c01135
ACS Omega 2022, 7, 15982−15995

Table 4. The Functional Group Attribution of 1000−1800 cm^{-1} at Sampling Points 1−6

sample point	center (cm^{-1})	area	area%	structure
sample point 1	1031	26.917	18.72%	C−O−C bond stretching vibration of ethers
	1111	23.898	16.62%	C−O−C bond stretching vibration of ethers
	1157	25.341	17.62%	C−O−C bond stretching vibration of ethers
	1427	30.485	21.20%	bending vibration of methyl C−H bond
	1524	13.497	9.39%	aromatic hydrocarbon benzene ring skeleton vibration
	1564	6.946	4.83%	aromatic hydrocarbon benzene ring skeleton vibration
	1629	10.224	7.11%	aromatic hydrocarbon benzene ring skeleton vibration
	1686	5.339	3.71%	C═O bond stretching vibration of aldehydes
	1744	1.164	0.81%	C═O bond stretching vibration of aldehydes
sample point 2	1028	18.147	16.96%	C−O−C bond stretching vibration of ethers
	1115	12.184	11.39%	C−O−C bond stretching vibration of ethers
	1160	15.062	14.08%	C−O−C bond stretching vibration of ethers
	1366	3.528	3.30%	O−H bond bending vibration of phenols
	1428	20.691	19.34%	Bending vibration of methyl C−H bond
	1482	16.282	15.22%	Aromatic hydrocarbon benzene ring skeleton vibration
	1548	7.341	6.86%	Aromatic hydrocarbon benzene ring skeleton vibration
	1626	9.311	8.70%	Aromatic hydrocarbon benzene ring skeleton vibration
	1696	4.436	4.15%	C═O bond stretching vibration of aldehydes
sample point 3	1035	6.333	4.55%	C−O−C bond stretching vibration of ethers
	1127	18.994	13.64%	C−O−C bond stretching vibration of ethers
	1158	13.627	9.79%	C−O−C bond stretching vibration of ethers
	1364	6.435	4.62%	O−H bond bending vibration of phenols
	1425	29.403	21.11%	bending vibration of methyl C−H bond
	1480	25.456	18.28%	aromatic hydrocarbon benzene ring skeleton vibration
	1542	13.649	9.80%	aromatic hydrocarbon benzene ring skeleton vibration
	1624	16.982	12.19%	aromatic hydrocarbon benzene ring skeleton vibration
	1695	8.377	6.02%	C═O bond stretching vibration of aldehydes
sample point 4	1027	21.786	18.80%	C−O−C bond stretching vibration of ethers
	1123	23.047	19.89%	C−O−C bond stretching vibration of ethers
	1154	16.555	14.29%	C−O−C bond stretching vibration of ethers
	1379	2.780	2.40%	O−H bond bending vibration of phenols
	1440	27.752	23.95%	bending vibration of methyl C−H bond
	1507	12.164	10.50%	aromatic hydrocarbon benzene ring skeleton vibration
	1621	9.018	7.78%	aromatic hydrocarbon benzene ring skeleton vibration
	1695	2.762	2.38%	C═O bond stretching vibration of aldehydes
sample point 5	1037	10.852	4.14%	C−O−C bond stretching vibration of ethers
	1125	35.182	13.41%	C−O−C bond stretching vibration of ethers
	1164	28.342	10.80%	C−O−C bond stretching vibration of ethers
	1357	10.440	3.98%	O−H bond bending vibration of phenols
	1416	42.578	16.23%	C−H bond bending vibration of olefins
	1460	45.954	17.52%	bending vibration of methyl C−H bond
	1506	29.265	11.16%	aromatic hydrocarbon benzene ring skeleton vibration
	1558	16.832	6.42%	aromatic hydrocarbon benzene ring skeleton vibration
	1622	24.693	9.41%	aromatic hydrocarbon benzene ring skeleton vibration
	1682	13.626	5.19%	C═O bond stretching vibration of aldehydes
	1738	4.580	1.75%	C═O bond stretching vibration of aldehydes
sample point 6	1036	16.338	10.66%	C−O−C bond stretching vibration of ethers
	1117	23.943	15.62%	C−O−C bond stretching vibration of ethers
	1163	21.150	13.80%	C−O−C bond stretching vibration of ethers
	1357	4.694	3.06%	O−H bond bending vibration of phenols
	1418	23.580	15.38%	C−H bond bending vibration of olefins
	1463	21.151	13.80%	bending vibration of methyl C−H bond
	1505	12.678	8.27%	aromatic hydrocarbon benzene ring skeleton vibration
	1555	7.960	5.19%	aromatic hydrocarbon benzene ring skeleton vibration
	1625	14.451	9.43%	aromatic hydrocarbon benzene ring skeleton vibration
	1693	7.346	4.79%	C═O bond stretching vibration of aldehydes

after gasification, while some easily volatile elements, such as mercury, will mostly migrate into the gas phase after undergoing high-temperature gasification reactions; only a small part remained in the ash. Moreover, since the raw coal undergoes complex physical and chemical changes upon underground gasification, the macromolecules in the coal easily crack to form

https://doi.org/10.1021/acsomega.2c01135
ACS Omega 2022, 7, 15982−15995

Table 5. Functional Group Attribution of 600−900 cm^{-1} at Sampling Points 7−12

sample point	center (cm^{-1})	area	area	structure
sample point 7	648	2.329	3.58%	Organic silicon compound Si−X stretching vibration
	671	5.223	8.02%	C−H bending vibration of benzene
	694	4.964	7.63%	C−H bending vibration of monosubstituted benzene
	713	6.714	10.32%	C−H bending vibration of m-disubstituted benzene
	730	6.938	10.66%	aromatic heterocyclic ring stretching vibration
	748	7.131	10.96%	C−H bending vibration of monosubstituted benzene
	766	7.570	11.63%	aromatic heterocyclic ring stretching vibration
	785	7.159	11.00%	C−H bending vibration of m-disubstituted benzene
	804	4.815	7.40%	aromatic heterocyclic ring stretching vibration
	825	3.569	5.48%	aromatic heterocyclic ring stretching vibration
	846	3.336	5.13%	C−H bending vibration of p-disubstituted benzene
	873	5.339	8.20%	C−H bending vibration of pentasubstituted benzene
sample point 8	648	3.283	4.57%	organic silicon compound Si−X stretching vibration
	672	5.709	7.95%	C−H bending vibration of benzene
	695	6.538	9.11%	C−H bending vibration of monosubstituted benzene
	717	9.043	12.59%	C−H bending vibration of m-disubstituted benzene
	737	8.837	12.31%	aromatic heterocyclic ring stretching vibration
	758	9.065	12.62%	C−H bending vibration of monosubstituted benzene
	777	8.735	12.17%	C−H bending vibration of m-disubstituted benzene
	797	7.009	9.76%	C−H bending vibration of m-disubstituted benzene
	820	3.873	5.39%	aromatic heterocyclic ring stretching vibration
	844	3.708	5.16%	C−H bending vibration of p-disubstituted benzene
	872	6.003	8.36%	C−H bending vibration of pentasubstituted benzene
sample point 9	650	3.243	5.46%	organic silicon compound Si−X stretching vibration
	676	5.867	9.88%	C−H bending vibration of benzene
	705	7.621	12.84%	C−H bending vibration of monosubstituted benzene
	730	9.501	16.01%	aromatic heterocyclic ring stretching vibration
	757	10.018	16.88%	C−H bending vibration of monosubstituted benzene
	784	9.100	15.33%	C−H bending vibration of m-disubstituted benzene
	808	5.004	8.43%	aromatic heterocyclic ring stretching vibration
	837	4.392	7.40%	C−H bending vibration of p-disubstituted benzene
	870	4.607	7.76%	C−H bending vibration of pentasubstituted benzene
sample point 10	649	2.656	3.38%	organic silicon compound Si−X stretching vibration
	671	6.515	8.30%	C−H bending vibration of benzene
	694	5.872	7.48%	C−H bending vibration of monosubstituted benzene
	713	8.095	10.31%	C−H bending vibration of m-disubstituted benzene
	730	8.502	10.83%	aromatic heterocyclic ring stretching vibration
	748	8.837	11.26%	C−H bending vibration of monosubstituted benzene
	766	9.680	12.33%	aromatic heterocyclic ring stretching vibration
	785	8.924	11.37%	C−H bending vibration of m-disubstituted benzene
	803	5.463	6.96%	aromatic heterocyclic ring stretching vibration
	825	3.788	4.82%	aromatic heterocyclic ring stretching vibration
	846	3.741	4.77%	C−H bending vibration of p-disubstituted benzene
	873	6.430	8.19%	C−H bending vibration of pentasubstituted benzene
sample point 11	650	8.445	4.81%	organic silicon compound Si−X stretching vibration
	674	13.490	7.69%	C−H bending vibration of benzene
	698	16.787	9.56%	C−H bending vibration of monosubstituted benzene
	721	26.202	14.93%	C−H bending vibration of m-disubstituted benzene
	743	24.909	14.19%	C−H bending vibration of monosubstituted benzene
	765	26.780	15.26%	aromatic heterocyclic ring stretching vibration
	789	24.372	13.89%	C−H bending vibration of m-disubstituted benzene
	814	10.940	6.23%	aromatic heterocyclic ring stretching vibration
	841	10.211	5.82%	C−H bending vibration of p-disubstituted benzene
	871	13.387	7.63%	C−H bending vibration of pentasubstituted benzene
sample point 12	649	9.255	5.64%	organic silicon compound Si−X stretching vibration
	676	16.043	9.78%	C−H bending vibration of benzene
	704	20.312	12.39%	C−H bending vibration of monosubstituted benzene
	729	26.777	16.33%	aromatic heterocyclic ring stretching vibration
	756	27.349	16.68%	C−H bending vibration of monosubstituted benzene
	782	25.573	15.60%	C−H bending vibration of m-disubstituted benzene
	805	14.765	9.00%	aromatic heterocyclic ring stretching vibration

https://doi.org/10.1021/acsomega.2c01135
ACS Omega 2022, 7, 15982−15995

Table 5. continued

sample point	center (cm^{-1})	area	area	structure
	836	11.362	6.93%	C−H bending vibration of p-disubstituted benzene
	870	12.541	7.65%	C−H bending vibration of pentasubstituted benzene

tiny molecular benzene rings, aliphatic chain hydrocarbons, aromatic hydrocarbons, tar, and other harmful pollutants. This complicates the composition of the resulting gas.[35−37]

From the area percentage of the sampling points 1−6 (Figure 12) obtained from the peak fitting diagram (Figure 11) and the functional group attribution table (Table 3), the Si−X bond of silicone compounds at sampling points 3 and 4 is smaller than that at the other four sampling points. This is because the sampling point is close to the wall of the simulated coal seam, and the temperature of the oxidation zone during the gasification process can reach more than 1000 °C. Under high temperatures, the silica in the simulated rock will react to break the Si−X bond.

Benzene compounds have high water solubility and are the typical organic pollutants produced during UCG. It can be seen from Figure 12 that the benzene compounds at sampling point 3 accounted for the largest proportion. This may be because sampling point No. 3 is close to the oxidation zone during the underground gasification process of the simulated coal seam. The high temperature will cause many cracks in the simulated rock layer.[38] Under the action of high temperature, the vapor of benzene compounds will migrate and diffuse along these cracks so that the proportion of benzene compounds in sampling point 3 is the highest. Sampling point No. 4 has the least percentage of benzene compounds. This is because the supply direction of the gasification agent is from south to north. Under the action of airflow, the high-temperature gas will carry these pollutants to migrate and enrich in the simulated strata. Therefore, sampling point No. 4 has less benzene than No. 5 and No. 6.

According to previous studies, aromatic heterocyclic compounds can also pollute groundwater. From Figure 12, it can be seen that the area percentage of the No. 4 sampling point is 35.29% and that it shows a downward trend. This is because the simulated rock layer has a certain degree of adsorption, resulting in the reduction of the pollutant content.

3.2.2.2. Sampling Points 1−6, 1000−1800 cm^{-1} Sub-Peak. Phenolic pollutants are typical pollutants produced upon underground gasification a high water solubility and migration tendency. Phenolic substances are produced in the process of UCG mainly from three aspects.[39−41] First, the coal used for gasification contains certain phenolic hydroxyl substances; Second, the gasification temperature is lower than that required for ether bond breaking (C−O−C), forming high-energy and unstable molecular fragments. These molecules will release their energy from relatively stable rings of phenol, alkyl phenol, and other phenols. When the gasification temperature was over 450 °C cracking happens and by alkyl phenol and secondary hydroxyl reactions, low-grade phenols with simple structure and small molecular weight were produced; Third, in the process of UCG, the temperature in the central zone of gasification can reach more than 1000 °C, and temperatures higher than that will make PAHs crack. Its products will react with oxygen-containing functional groups to produce phenolic substances.

According to the area percentage diagram (Figure 14) of sampling points 1−6 obtained from the peak fitting diagram (Figure 13) and the functional group attribution table (Table 4), the proportion of phenolic pollutants at sampling point 3 is the largest and shows a decreasing trend to the south. Moreover, no phenolic pollutants were detected at sampling point 1. This indicates that the phenolic pollutants migrate and diffuse to the simulated rock layer around the simulated coal seam. The maximum vertical distance of migration and diffusion from the gasification reaction area to the south is about 0.7 m. Campbell's research found that aromatic hydrocarbons are also organic pollutants produced by UCG. It can be seen from Figure 14 that the maximum percentage of aromatic pollutants at sampling point 3 is 40.27%. After that, it shows a downward trend along with the simulated rock formation to the south and shows a trend of the first decline and then increase toward the north. Compared with phenolic pollutants, the migration and diffusion distance of aromatic pollutants is higher than that of phenolic pollutants, which indicates that the simulated rock layer has a strong adsorption for phenolic pollutants, leading to a smaller migration distance. This is consistent with the results of XRD.

3.2.2.3. Sampling Points 7−12, 600−900 cm^{-1} Sub-Peak. From the area percentage diagram of sampling points 7−12 (Figure 16) obtained from the peak fitting diagram (Figure 15) and the functional group attribution table (Table 5), the change in Si−X bond at sampling points 7−9 and 10−12 is consistent with that at sampling points 1−6. In contrast, the change in benzene and aromatic heterocyclic compounds is different. Sampling points 7 and 10 are located on both sides of the simulated coal seam, 10 cm away from the coal wall, and are in the central area of the gasification reaction. Under heat, the cracks developed in the simulated rock layer provide channels for the migration of the gaseous pollutants. During the gasification process, if the gasification agent is injected at a pressure not less than the hydrostatic pressure of the coal seam, the gas generated by the gasification process will penetrate the surrounding formation media through these fissures and cause pollution. From the percentage of area shown in Figure 16, it can be seen that the benzene and aromatic heterocyclic compounds show opposite trends. This shows that benzene pollutants migrate and enrich easily than aromatic heterocyclic compounds.

(4) Sampling points 7−12, 1000−1800 cm^{-1} sub-peak.

The gas produced by UCG contains a lot of macromolecular organic matter produced by coal pyrolysis. The more the volatile products are produced, the farther they penetrate the surrounding rock layers before dissolving into groundwater. There are three main sources for the formation of PAHs during the UCG process.[42−44] First, the raw coal itself contains a small amount of PAHs. Under the gasification conditions, inevitably there will be some PAHs that do not react and are discharged with coal gas and semicoke. Second, under high temperatures, the olefin and alkyne generated by coal decomposition continue to decompose into free radical groups. These free radical groups will form low-grade aromatic rings after dehydrogenation and recombination, which will further polymerize to generate PAHs. Third, coal molecules are a network structure, which will be decomposed into small molecules without rings and with a ring under gasification conditions. After the cyclization reaction, the small molecules without rings can also produce PAHs.

From the area percentage diagram of sampling points 7−12 obtained from the peak fitting diagram (Figures 17 and 18) and

https://doi.org/10.1021/acsomega.2c01135
ACS Omega 2022, 7, 15982−15995

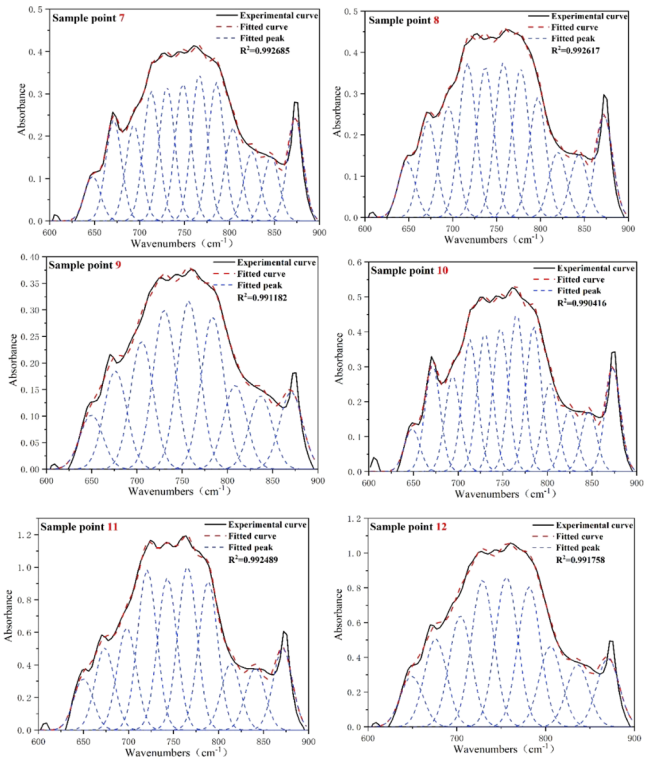

Figure 15. Fitting curve of 600−900 cm^{-1} at sampling points 7−12.

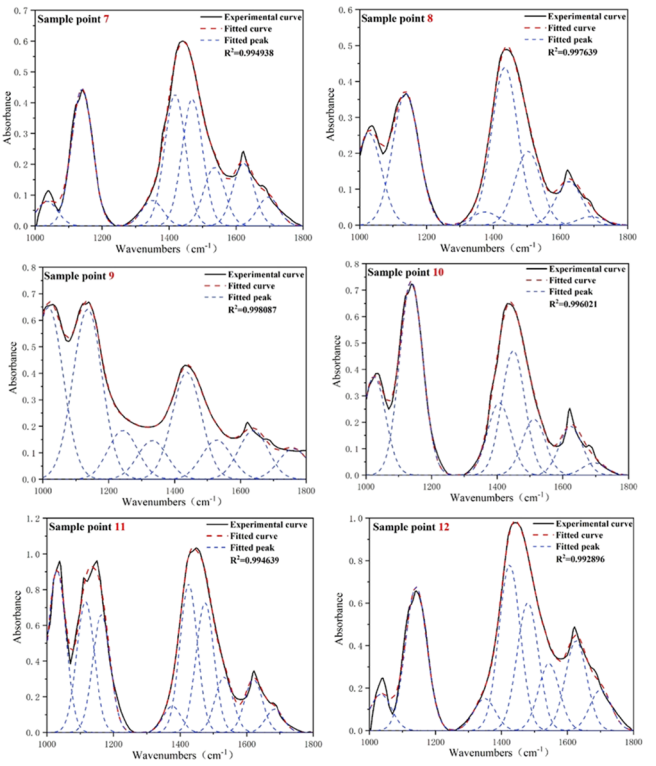

Figure 17. Fitting curve of 1000−1800 cm^{-1} sampling points 7−12.

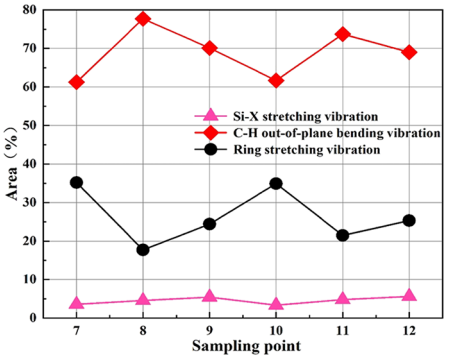

Figure 16. 600−900 cm^{-1} percentage of area.

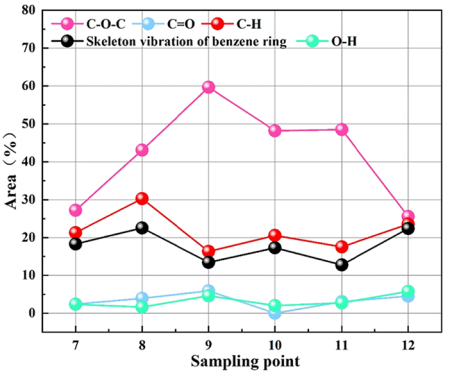

Figure 18. 1000−1800 cm^{-1} percentage of area.

the functional group attribution table (Table 6), it can be seen that the change in aromatic hydrocarbon pollutants first decreases and then increases from the gasification center area to the east, while it is just the opposite to the west. The area percentage of phenols and aldehydes from the gasification reaction center to the east and west sides shows an increasing trend. The area percentage of the two pollutants is roughly the same. This shows that the phenol and aldehyde migration and enrichment degree is roughly the same on the east and west sides.

4. PREVENTION AND CONTROL OF POLLUTANTS

The generation, migration, and enrichment of UCG pollutants mainly depend on the fracture development pattern of the surrounding rock under the thermal action during gasification, the adsorption characteristics of the surrounding rock, the extension of the gasification working surface, the gas injection pressure, and the elemental composition of the coal. Therefore, in the actual production stage, the detailed study of the elemental composition of gasified coal, the scientific site selection of the gasified coalfield, and the selection of gasification technology are very important to prevent pollution by UCG.

The following measures can be taken to prevent and control this problem: (1) Scientific site selection before gasification. Before gasification, the condition of the gasification coal seam should be fully evaluated and there should be a certain thickness of dense water-proof layer between it and the underground aquifer. The gasification area should not contain important aquifers (poor water quality, less water volume, and environmental and economically important aquifers) and the groundwater area of the gasification area should be at a low point than the regional groundwater level. (2) Scientific process control during gasification. In the process of gasification, gaseous pollutants mainly migrate and escape along with the gas and hence the gasification pressure should be controlled to be less than or equal to the hydrostatic pressure of the coal seam to seal the pollutants in the gasification reaction zone to reduce the diffusion of pollutants. (3) Pollutant treatment after gasification.

https://doi.org/10.1021/acsomega.2c01135
ACS Omega 2022, 7, 15982−15995

Table 6. The Functional Group Attribution of 1000−1800 cm^{-1} at Sampling Points 7−12

sample point	center (cm^{-1})	area	area	structure
sample point 7	1036	6.241	4.13%	C−O−C bond stretching vibration of ethers
	1140	34.830	23.04%	C−O−C bond stretching vibration of ethers
	1350	6.473	4.28%	O−H bond bending vibration of phenols
	1418	33.388	22.09%	C−H bond bending vibration of olefins
	1469	32.141	21.26%	bending vibration of methyl C−H bond
	1535	14.837	9.82%	aromatic hydrocarbon benzene ring skeleton vibration
	1622	15.922	10.53%	aromatic hydrocarbon benzene ring skeleton vibration
	1696	7.323	4.84%	C═O bond stretching vibration of aldehydes
sample point 8	1027	25.089	17.74%	C−O−C bond stretching vibration of ethers
	1138	35.816	25.33%	C−O−C bond stretching vibration of ethers
	1375	3.557	2.52%	O−H bond bending vibration of phenols
	1434	42.766	30.25%	bending vibration of methyl C−H bond
	1503	20.029	14.17%	aromatic hydrocarbon benzene ring skeleton vibration
	1625	11.837	8.37%	aromatic hydrocarbon benzene ring skeleton vibration
	1691	2.280	1.63%	C═O bond stretching vibration of aldehydes
sample point 9	1017	72.855	26.27%	C−O−C bond stretching vibration of ethers
	1135	71.977	25.95%	C−O−C bond stretching vibration of ethers
	1243	20.655	7.45%	C−O−C bond stretching vibration of ethers
	1332	16.397	5.91%	O−H bond bending vibration of phenols
	1437	45.290	16.33%	bending vibration of methyl C−H bond
	1528	16.645	6.00%	aromatic hydrocarbon benzene ring skeleton vibration
	1639	20.632	7.44%	aromatic hydrocarbon benzene ring skeleton vibration
	1761	12.898	4.65%	C═O bond stretching vibration of aldehydes
sample point 10	1026	32.803	16.25%	C−O−C bond stretching vibration of ethers
	1138	64.487	31.94%	C−O−C bond stretching vibration of ethers
	1406	24.129	11.95%	bending vibration of alkane C−H Bond
	1449	41.464	20.54%	bending vibration of methyl C−H bond
	1512	18.661	9.24%	aromatic hydrocarbon benzene ring skeleton vibration
	1625	16.228	8.04%	aromatic hydrocarbon benzene ring skeleton vibration
	1696	4.1247	2.04%	C═O bond stretching vibration of aldehydes
sample point 11	1030	60.900	19.16%	C−O−C bond stretching vibration of ethers
	1116	49.055	15.43%	C−O−C bond stretching vibration of ethers
	1164	44.228	13.91%	C−O−C bond stretching vibration of ethers
	1376	9.849	3.10%	O−H bond bending vibration of phenols
	1426	55.766	17.54%	bending vibration of methyl C−H bond
	1475	48.729	15.33%	bending vibration of C−H bond of methine
	1532	20.786	6.54%	aromatic hydrocarbon benzene ring skeleton vibration
	1621	19.838	6.24%	aromatic hydrocarbon benzene ring skeleton vibration
	1684	8.771	2.76%	C═O bond stretching vibration of aldehydes
sample point 12	1035	13.863	5.17%	C−O−C bond stretching vibration of ethers
	1141	54.710	20.40%	C−O−C bond stretching vibration of ethers
	1349	12.218	4.55%	O−H bond bending vibration of phenols
	1425	63.164	23.55%	bending vibration of methyl C−H bond
	1479	48.743	18.17%	bending vibration of C−H bond of methane
	1544	25.671	9.57%	aromatic hydrocarbon benzene ring skeleton vibration
	1626	34.322	12.80%	aromatic hydrocarbon benzene ring skeleton vibration
	1700	15.550	5.80%	C═O bond stretching vibration of aldehydes

After gasification, the generation of pollutants can be reduced by accelerating the cooling of the combustion cavity to suppress pressure rise. Pumping polluted water from the combustion area and the surrounding strata to the ground for treatment effectively removes highly mobile pollutants.[45−47]

5. CONCLUSIONS

According to the analysis and detection of coal seam surrounding rock under the gasification simulation experiment of No. 7 coal in Tianjin Qianjiaying Mine, the following conclusions can be drawn:

(1) After underground gasification and the high-temperature reaction of Qianjiaying No. 7 coal seam, benzene, phenols, aldehydes, aromatic hydrocarbons, and aromatic heterocyclic compounds were found through the detection of the surrounding rock around the coal seam, of which aromatic pollutants are the main pollutants.

(2) On the east and west sides of the gasification center, the migration and enrichment of phenols and aldehydes are roughly the same. At the same time, benzene pollutants are easier to migrate and enrich than aromatic heterocyclic compounds, which indicates that the prevention and control of benzene pollutants should be

https://doi.org/10.1021/acsomega.2c01135
ACS Omega 2022, 7, 15982−15995

strengthened during actual gasification production to reduce their pollution around the fuel−air area.

(3) In the south of the gasification area, the migration distance of phenolic pollutants is less than that of other pollutants. The maximum vertical distance of its migration and diffusion from the gasification reaction area to the south is about 0.7 m.

(4) Before proceeding to UCG, a detailed study of the elemental composition of the gasified coal, scientific selection of the gasification coalfield, and scientific selection of the gasification process are very important links in preventing pollution by UCG.

AUTHOR INFORMATION

Corresponding Author

Lin Xin − *College of Safety and Environmental Engineering and Key Laboratory of Ministry of Education for Mine Disaster Prevention and Control, Shandong University of Science and Technology, Qingdao, Shandong 266590, China*; Email: xinlinsdust@sdust.edu.cn

Authors

Kaixuan Li − *College of Safety and Environmental Engineering, Shandong University of Science and Technology, Qingdao, Shandong 266590, China*; orcid.org/0000-0002-4589-8593

Mingze Feng − *College of Safety and Environmental Engineering, Shandong University of Science and Technology, Qingdao, Shandong 266590, China*

Weimin Cheng − *College of Safety and Environmental Engineering and Key Laboratory of Ministry of Education for Mine Disaster Prevention and Control, Shandong University of Science and Technology, Qingdao, Shandong 266590, China*

Zhigang Wang − *North China Geological Exploration Bureau of Tianjin, Tianjin 300170, China*

Jiaze Li − *College of Safety and Environmental Engineering, Shandong University of Science and Technology, Qingdao, Shandong 266590, China*

Jing Wu − *College of Safety and Environmental Engineering, Shandong University of Science and Technology, Qingdao, Shandong 266590, China*

Complete contact information is available at: https://pubs.acs.org/10.1021/acsomega.2c01135

Notes

The authors declare no competing financial interest.

ACKNOWLEDGMENTS

This study was financially supported by the Shandong Natural Science Foundation (No. ZR2020ME084), the National Natural Science Foundation of China (No. 51504142), the Qingchuang Science and Technology Program of Shandong Province University (No. 2019KJG008), the SDUST Research Fund (No. 2018TDJH102), and the Geological Survey Project of China Geological Survey (No. DD20190182).

REFERENCES

(1) Han, S.; Chen, H.; Long, R.; Cui, X. Peak coal in China: A literature review. *Resour., Conserv. Recycl.* **2018**, *129*, 293−306.

(2) Wang, J.; Dong, X.; Dong, K. How renewable energy reduces CO_2 emissions? Decoupling and decomposition analysis for 25 countries along the Belt and Road. *Appl. Econ.* **2021**, *53*, 4597−4613.

(3) Heede, R.; Oreskes, N. Potential emissions of CO_2 and methane from proved reserves of fossil fuels: An alternative analysis. *NATO ASI Ser., Ser. I* **2016**, *36*, 12−20.

(4) Liu, H.; Liu, S. Life cycle energy consumption and GHG emissions of hydrogen production from underground coal gasification in comparison with surface coal gasification. *Int. J. Hydrogen Energy* **2021**, *46*, 9630−9643.

(5) Krause, E.; Krzemień, A.; Smoliński, A. Analysis and assessment of a critical event during an underground coal gasification experiment. *J. Loss Prev. Process Ind.* **2015**, *33*, 173−182.

(6) Bazaluk, O.; Lozynskyi, V.; Falshtynskyi, V.; Saik, P.; Dychkovskyi, R.; Cabana, E. Experimental studies of the effect of design and technological solutions on the intensification of an underground coal gasification process. *Energies* **2021**, *14*, 4369.

(7) Jiang, L.; Chen, Z.; Ali, S. M. F. Feasibility of carbon dioxide storage in post-burn underground coal gasification cavities. *Appl. Energy* **2019**, *252*, No. 113479.

(8) Falshtynskyi, V.; Saik, P.; Lozynskyi, V.; Dychkovskyi, R.; Petlovanyi, M. Innovative aspects of underground coal gasification technology in mine conditions. *Mining of Mineral Deposits* **2018**, *12*, 68−75.

(9) Huang, W.; Wang, Z.; Xie, T.; Du, X. Feasibility study on underground coal gasification of quality characteristics of 9 Chinese coal types. *Energy Sources, Part A* **2020**, *42*, 131−152.

(10) Škvareková, E.; Tomašková, M.; Wittenberger, G.; Zelenák, Š. Analysis of risk factors for underground coal gasification. *Management Systems in Production Engineering* **2019**, *27*, 227−235.

(11) Zou, C.; Chen, Y.; Kong, L.; Sun, F.; Chen, S.; Dong, Z. Underground coal gasification and its strategic significance to the development of natural gas industry in China. *Pet. Explor. Dev.* **2019**, *46*, 205−215.

(12) Xin, L.; Li, J.; Xie, J.; Li, C.; Han, L.; An, M.; Xu, M.; Wang, Z. Simulation of cavity extension formation in the early ignition stage based on a coal block gasification experiment. *ASME: J. Energy Resour. Technol.* **2020**, *142*, No. 062304.

(13) Strugala-Wilczek, A.; Stanczyk, K. Comparison of metal elution from cavern residue after underground coal gasification and from ash obtained during coal combustion. *Fuel* **2015**, *158*, 733−743.

(14) Li, J.-G.; Gao, B.-P.; Wang, Y.-Y.; Wei, H.-R.; Zhao, J. Experimental reserach on pollutants precipitation of underground coal gasification. *J. China Coal Soc.* **2012**, *37*, 173−177.

(15) Kapusta, K.; Stańczyk, K.; Wiatowski, M.; Chećko, J. Environmental aspects of a field-scale underground coal gasification trial in a shallow coal seam at the Experimental Mine Barbara in Poland. *Fuel* **2013**, *113*, 196−208.

(16) Ütnü, Y. E.; Okutan, H.; Aydın, A. A. Polycyclic aromatic hydrocarbon (PAH) content of Malkara lignite and its ex-situ underground coal gasification (UCG) char residues. *Fuel* **2020**, *275*, No. 117949.

(17) Ma, W.; Liu, S.; Li, Z.; Lv, J.; Yang, L. Release and transformation mechanisms of hazardous trace elements in the ash and slag during underground coal gasification. *Fuel* **2020**, *281*, No. 118774.

(18) Liu, S.; Niu, M.; Qi, K.; Song, X.; Li, J.; He, Y.; Wang, Z.; Gao, B. Migration behavior of typical pollutants from underground coal gasification. *J. China Coal Soc.* **2018**, *43*, 2618−2624.

(19) Ye, Y.; Chen, L.; Xing, B.; Yi, G.; Xu, B.; Li, Z.; Zhang, L. Research on the pollution from underground bituminous coal gasification. *Applied Chemical Industry* **2016**, *45*, 1424−1427+1430.

(20) Liu, S.; Ma, W. Leaching characteristics of hazardous trace elements in the slag from oxygen-enriched underground coal gasification. *J. China Coal Soc.* **2020**, *45*, 4201−4208.

(21) Li, Z.-X.; Chen, L.-J.; Ye, Y.-N.; Xu, B.; Liu, K.; Zhang, L.; Liu, J.-W.; Su, Y. Dissolution of pollutants from large semi-coke particles in groundwater. *Chem. Eng.* **2016**, *44*, 58−63.

(22) Sadasivam, S.; Zagorščak, R.; Thomas, H. R.; Kapusta, K.; Stańczyk, K. Characterisation of the Contaminants Generated from a Large-Scale Ex-Situ Underground Coal Gasification Study Using High-Rank Coal from the South Wales Coalfield Water, Air, & Soil Pollution: An International. *J. Environ. Pollut.* **2020**, *231*, 43−51.

https://doi.org/10.1021/acsomega.2c01135
ACS Omega 2022, 7, 15982−15995

(23) Chen, L.; Li, C.; Xu, B.; Xing, B.; Yi, G.; Huang, G.; Zhang, C.; Liu, J. Microbial degradation of organic pollutants in groundwater related to underground coal gasification. *Energy Sci. Eng.* **2019**, *7*, 2098−2111.
(24) Hou, G.; Liang, J.; Jing, H.; Tan, J.; Zhang, Y.; Yang, X.; Xie, X. Influence of Deviatoric Stress on the Deformation and Damage Evolution of Surrounding Rock under Unloading Conditions. *Shock and Vibration* **2020**, *2020*, 1−14.
(25) An, W.; Wang, L.; Liu, X.; Pan, J.; Li, X. Analysis the Structural Characteristics of Fuxin Long Flane Coal Based on FTIR and XRD Experiments. *Polym. Bull.* **2018**, *3*, 67−74.
(26) Li, Q.; Lin, B.; Zhao, C.; Wu, W. Chemical Structure Analysis of Coal Char Surface Based on Fourier-Transform Infrared Spectrometer. *Proc. CSEE* **2011**, *31*, 46−52.
(27) Imran, M.; Kumar, D.; Kumar, N.; Qayyum, A.; Saeed, A.; Bhatti, M. S. Environmental concerns of underground coal gasification. *Renewable Sustainable Energy Rev.* **2014**, *31*, 600−610.
(28) Xu, B.; Chen, L.; Xing, B.; Li, L.; Zhang, L.; Wang, X.; Chen, H.; Yi, G.; Huang, G. The environmental effect of underground coal gasification semiâ coke on confined groundwater. *Environ. Prog. Sustainable Energy* **2016**, *35*, 1584−1589.
(29) Mellors, R.; Yang, X.; White, J. A.; Ramirez, A.; Wagoner, J.; Camp, D. W. Advanced geophysical underground coal gasification monitoring. *Mitig. Adapt. Strateg. Glob. Change* **2016**, *21*, 487−500.
(30) Xu, M.; Xin, L.; Liu, W.; Hu, X.; Cheng, W.; Li, C.; Wang, Z. Study on the physical properties of coal pyrolysis in underground coal gasification channel. *Powder Technol.* **2020**, *376*, 573−592.
(31) Agarwal, M.; Kudapa, V. K.; Sudharsan, J. Analytical study of structural characteristics of South Eastern coal field by FTIR spectroscopy and X-ray diffraction. *Mater. Today: Proc.* **2021**, *47*, 5319−5325.
(32) Zhang, Y.; Wang, J.; Xue, S.; Wu, J.; Chang, L.; Li, Z. Kinetic study on changes in methyl and methylene groups during low-temperature oxidation of coal via in-situ FTIR. *Int. J. Coal Geol.* **2016**, *154*, 155−164.
(33) Akbarzadeh, H.; Chalaturnyk, R. J. Structural changes in coal at elevated temperature pertinent to underground coal gasification: A review. *Int. J. Coal Geol.* **2014**, *131*, 126−146.
(34) Smoliński, A.; Stańczyk, K.; Kapusta, K.; Howaniec, N. Chemometric Study of the Ex Situ Underground Coal Gasification Wastewater Experimental Data. *Water, Air, Soil Pollut.* **2012**, *223*, 5745−5758.
(35) Pankiewicz-Sperka, M.; Stańczyk, K.; Płaza, G. A.; Kwaśniewska, J.; Nałącz-Jawecki, G. Assessment of the chemical, microbiological and toxicological aspects of post-processing water from underground coal gasification. *Ecotoxicol. Environ. Saf.* **2014**, *108*, 294−301.
(36) Ma, W.; Li, Z.; Lv, J.; Yang, L.; Liu, S. Environmental evaluation study of toxic elements (F, Zn, Be, Ni, Ba, U) in the underground coal gasification (UCG) residuals. *J. Cleaner Prod.* **2021**, *297*, No. 126565.
(37) Durdán, M.; Laciak, M.; Kačur, J.; Flegner, P.; Kostúr, K. Evaluation of synthetic gas harmful effects created at the underground coal gasification process realized in laboratory conditions. *Measurement* **2019**, *147*, No. 106866.
(38) Xin, L.; Li, C.; Liu, W.; Xu, M.; Xie, J.; Han, L.; An, M. Change of sandstone microstructure and mineral transformation nearby UCG channel. *Fuel Process. Technol.* **2021**, *211*, No. 106575.
(39) Zheng, M.; Li, X.; Guo, L. Dynamic trends for char/soot formation during secondary reactions of coal pyrolysis by large-scale reactive molecular dynamics. *J. Anal. Appl. Pyrolysis* **2021**, *155*, No. 105048.
(40) Wang, G.; Zhou, A. Time evolution of coal structure during low temperature air oxidation. *Int. J. Min. Sci. Technol.* **2012**, *22*, 517−521.
(41) Richter, H.; Howard, J. B. Formation of polycyclic aromatic hydrocarbons and their growth to soot-a review of chemical reaction pathways. *Prog. Energy Combust. Sci.* **2000**, *26*, 565−608.
(42) Sun, J.; Feng, H.; Xu, J.; Jin, H.; Guo, L. Investigation of the conversion mechanism for hydrogen production by coal gasification in supercritical water. *Int. J. Hydrogen Energy* **2021**, *46*, 10205−10215.
(43) Deming, W.; Xiaoxing, Z.; Junjie, G.; Xuyao, Q. Changes in active functional groups during low-temperature oxidation of coal. *Min. Sci. Technol.* **2010**, *20*, 35−40.
(44) Korenaga, T.; Liu, X.; Huang, Z. The influence of moisture content on polycyclic aromatic hydrocarbons emission during rice straw burning. *Chemosphere: Global Change Sci.* **2001**, *3*, 117−122.
(45) Khadse, A. N. Resources and economic analyses of underground coal gasification in India. *Fuel* **2015**, *142*, 121−128.
(46) Wang, G. X.; Wang, Z. T.; Feng, B.; Rudolph, V.; Jiao, J. L. Semi-industrial tests on enhanced underground coal gasification at Zhong-Liang-Shan coal mine. *Asia-Pac. J. Chem. Eng.* **2009**, *4*, 771−779.
(47) Xin, L.; Wang, Z.; Wang, G.; Nie, W.; Zhou, G.; Cheng, W.; Xie, J. Technological aspects for underground coal gasification in steeply inclined thin coal seams at Zhongliangshan coal mine in China. *Fuel* **2019**, *191*, 486−494.

https://doi.org/10.1021/acsomega.2c01135
ACS Omega 2022, 7, 15982−15995